Science Advances

AAAS

advances.sciencemag.org/cgi/content/full/2/11/e1601113/DC1

Supplementary Materials for

Complex formation dynamics in a single-molecule electronic device

Huimin Wen, Wengang Li, Jiewei Chen, Gen He, Longhua Li, Mark A. Olson, Andrew C.-H. Sue, J. Fraser Stoddart, Xuefeng Guo

Published 25 November 2016, *Sci. Adv.* **2**, e1601113 (2016)
DOI: 10.1126/sciadv.1601113

This PDF file includes:

Supplementary Materials and Methods

1. General Methods

All reagents and starting materials were purchased from Aldrich and used without further purification. All reactions were performed under an N_2 atmosphere and in dry solvents unless otherwise noted. ^{1}H and ^{13}C NMR Spectra were measured on either a Bruker Avance III 400 MHz or a Bruker Avance III 600 MHz spectrometer at ambient temperature unless otherwise stated. Chemical shifts are listed in ppm on the scale and coupling constants are recorded in Hertz (Hz). Chemical shifts are reported in ppm relative to the signals corresponding to the residue non-deuterated solvents ($CDCl_3$: δ = 7.26 ppm, CD_3SOCD_3: δ = 2.50 ppm, D_2O: δ = 4.79 ppm). The following abbreviations are used to explain the multiplicities: s, singlet; d, doublet; t, triplet; b, broad peaks; m, multiplet or overlapping peaks. HR-MS (ESI) Spectra were performed on a Bruker Apex IV FT-MS spectrometer.

2. Synthetic Methods

Chemicals were purchased from commercial vendors and used as received without further purification unless otherwise noted. OPEDAM (*40*) (fig. S6d) and BPP34C10DA (*44*, *45*) were synthesized as reported previously.

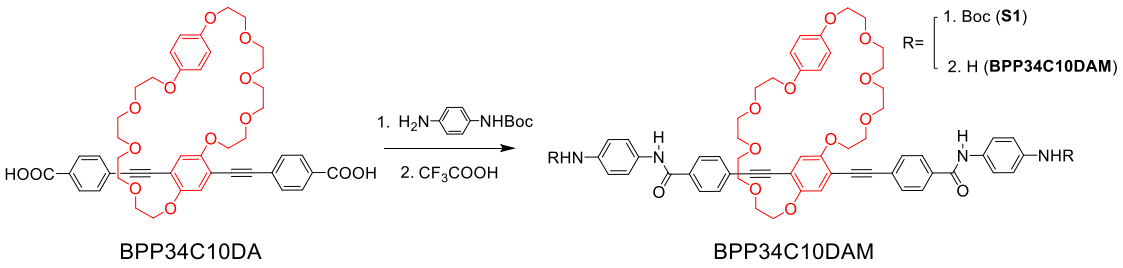

scheme S1. Synthesis of BPP34C10DAM from BPP34C10DA. 1) EDCI coupling reaction with 4-(*t*-butoxycarbonylamino) aniline, 2) *N*-Boc deprotection reaction with CF_3COOH.

S1: A mixture of BPP34C10DA (100 mg, 0.12 mmol), 4-(*t*-butoxycarbonylamino) aniline (25.2 mg, 0.12 mmol) and 1-ethyl-3-(3-dimethylaminopropyl) carbodiimide hydrochloride (EDCI) (37.3 mg, 0.24 mmol) in a 1:1 (v/v) mixture of THF/CH_2Cl_2 (10 mL) was stirred for 24 h at room temperature. The sol vent was then removed under vacuum and the residue was purified by column chromatography (SiO_2) using MeOH/CH_2Cl_2 (1:19 v/v) as the eluent. The purified S1 (109 mg, 75%) is a yellow solid. ^{1}H-NMR ($CDCl_3$, 400 MHz, 298 K): δ = 7.87 (s, 2H), 7.85 (d, J = 8.4 Hz, 4H),

7.63 (d, J = 8.4 Hz, 4H), 7.59 (d, J = 8.4 Hz, 4H), 7.39 (d, J = 8.4 Hz, 4H), 7.03 (s, 2H), 6.68 (s, 4H), 6.47 (s, 2H), 4.13−3.63 (m, 16H), 1.53 (s, 18H). ^{13}C NMR ($CDCl_3$, 100 MHz, 298 K): δ = 165.1, 154.0, 153.1, 153.0, 135.3, 134.5, 133.3, 132.0, 127.3, 127.0, 121.3, 119.4, 117.4, 115.7, 114.4, 94.7, 88.6, 80.7, 71.3, 71.1, 71.0, 70.9, 69.9, 69.9, 68.3, 68.1, 28.5. HR-MS (ESI): calcd. for $C_{68}H_{76}N_4O_{16}$ m/z = 1227.5154 $[M + Na]^+$, found m/z = 1227.5138 $[M + Na]^+$, m/z =1205.5335 $[M + H]^+$, found m/z =1205.5309 $[M + H]^+$.

BPP34C10DAM: S1 (100 mg, 0.083 mmol) was dissolved in a 1:1 (v/v) mixture of CF_3COOH/CH_2Cl_2 (10 mL) and stirred for 2 h. The mixture was rendered basic by the addition of NH_4OH and extracted with CH_2Cl_2. The organic phase was dried ($MgSO_4$) and then concentrated to yield **BPP34C10DAM** as a yellow solid (80.1 mg, 96 %). ^{1}H-NMR ($CDCl_3$, 400 MHz, 298 K): δ = 7.84 (d, J = 8.4 Hz, 4H), 7.77 (s, 2H), 7.62 (d, J = 8.4 Hz, 4H), 7.42 (d, J = 8.4 Hz, 4H), 7.02 (s, 2H), 6.70 (d, J = 8.4 Hz, 4H), 6.68 (s, 4H), 4.18−3.63 (m, 16H). ^{13}C NMR ($CDCl_3$, 100 MHz, 298 K): δ =165.0, 153.9, 153.0, 143.7, 134.7, 131.9, 129.4, 127.2, 126.7, 122.4, 117.2, 116.9, 115.6, 114.2, 94.7, 88.4, 71.2, 71.0, 70.9, 70.8, 69.9, 69.7, 68.2, 29.8. HR-MS (ESI): calcd. for $C_{58}H_{60}N_4O_{12}$ m/z = 1043.3845 $[M + K]^+$, found m/z =1043.3828 $[M + K]^+$, m/z = 1005.4286 $[M + H]^+$, found m/z = 1005.4282 $[M + H]^+$.

3. Fabrication Processes of Single-Molecule Junction (SMJ) Devices

Device fabrication and molecular connection

Identical high-density graphene field-effect transistor (FET) arrays were produced following a previously described method (*32*) (figs. S1 and S2). Briefly, high-quality single-layered graphene (SLG) was grown on copper films by a chemical vapor deposition (CVD) procedure. By using a nondestructive PMMA-mediated transfer technique, SLG was transferred to a silicon substrate. Through two photolithographic processes, high-density patterned metallic electrodes (8 nm of Cr followed by 60 nm of Au) separated by 7 μm were deposited onto SLG sheets by thermal evaporation to form graphene FET arrays. Note that for a 50 nm-thick silicon oxide layer (SiO_2, the light brown part of graphene devices in Fig. 1) was deposited by electron beam thermal evaporation after resistance thermal deposition of patterned metallic electrodes. The SiO_2 passivation layers on the gold electrode surfaces prevent any direct contact and leakage between the solution and the metal electrodes during the subsequent electrical measurements in Me_2SO or aqueous solution.

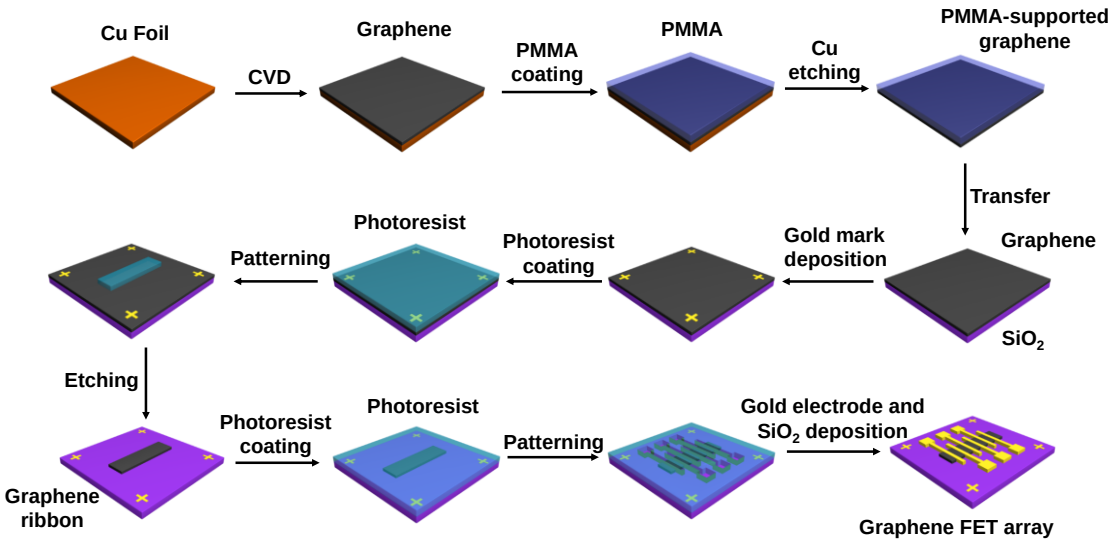

fig. S1. Schematic representation of the fabrication procedure to form graphene field-effect transistor arrays.

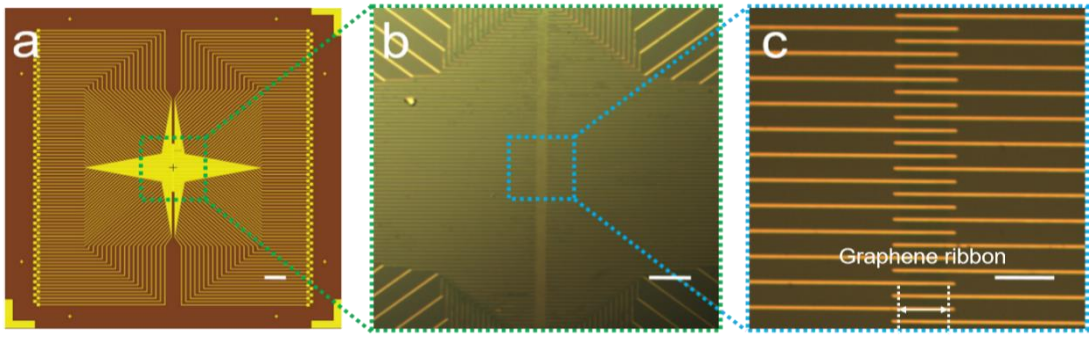

fig. S2. Optical microscopic images of graphene devices with different magnification. The yellow part is deposited gold electrodes (Cr/Au: 8/60 nm), and the central part under the gold electrodes is graphene ribbon (40 × 150 μm^2). Scale bar: a, 1 mm; b, 100 μm; c, 40 μm.

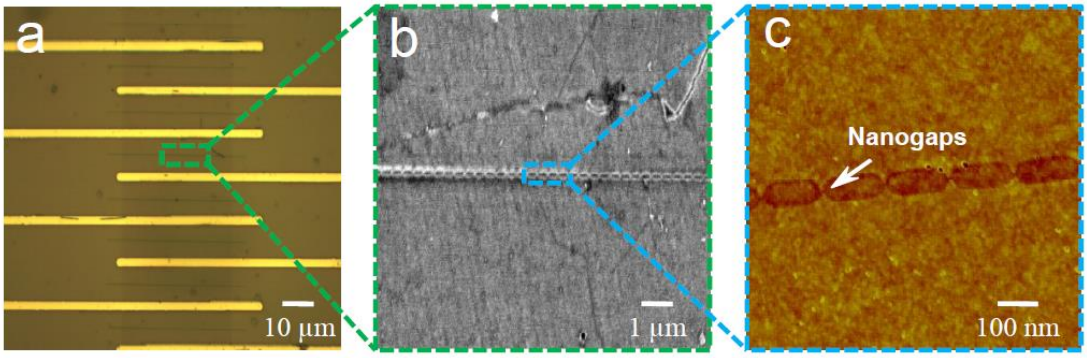

fig. S3. Characterization of an indented nanogap array. (**a**) Optical image of graphene FETs located in the center of each pattern after electron beam lithography and oxygen plasma etching. (**b**) and (**c**) High-resolution SEM and AFM images of a representative indented graphene point contact array.

Following graphene FET fabrication, by using ultrahigh-resolution electron beam lithography (*32*, *33*), a DesignCAD file with a 5 nm-width dash line was adopted to open a window precursor in a spin-cast layer of polymethylmethacrylate (PMMA). After the window had been opened, the devices were put into an ME-3A RIE machine. The graphenes were then locally cut through the open window by oxygen plasma. After cutting, the devices were soaked in Me_2CO overnight, removed, washed by Me_2CO, *i*-PrOH and DI H_2O, and dried with a stream of N_2 gas. An indented nanogap array was formed (fig. S3) on the graphene layer between two adjacent gold electrodes, resulting in graphene open circuits with carboxylic acid-terminated graphene point contacts (Fig. 1A) that were applied as the platform for the following SMJ investigations.

After the lithographic process, the freshly prepared graphene point contact array devices (five sets in total) were immersed in a pyridine solution with 0.1 mM of BPP34C10DAM for coupling reactions with 1 mM EDCI. After leaving them to react for 48 h, the devices were removed from the solution and rinsed with deionized H_2O and Me_2CO several times before being dried with a N_2 stream. The as-prepared SMJ devices were ready for solid-state characterization and $MV{\cdot}2PF_6$ addition.
For $MV{\cdot}2PF_6$ addition, the BPP34C10-SMJ devices were immersed into a 1 mM Me_2SO solution of $MV{\cdot}2PF_6$ for 12 h. The devices were removed from solution, rinsed with deionized H_2O and Me_2CO, and then dried with a N_2 stream prior to electrical characterization.

4. Solid-State Characterization

Electrical characterization

Solid-state electrical characterization (*I-V* and *I-t*) (fig. S4) was carried out at room temperature in ambient atmosphere with the use of an Agilent 4155C semiconductor parameter system (DC measurements) and a Karl Suss (PM5) manual probe station.

After being immerged in a Me_2SO solution of 1 mM $MV{\cdot}2PF_6$ for 12 h, $MV^{2+}\subset$BPP34C10-SMJ were rinsed, dried, and tested in the solid state (Fig. 1C). The electric current passing through SMJs showed approximately one order of magnitude increase on average (figs. S4 and S5, a and b), which is presumably attributed to the host-guest complexation between a MV^{2+} cation and the BPP34C10 macrocycle in the SMJ, forming the $MV^{2+}\subset$BPP34C10 psuedorotaxane.

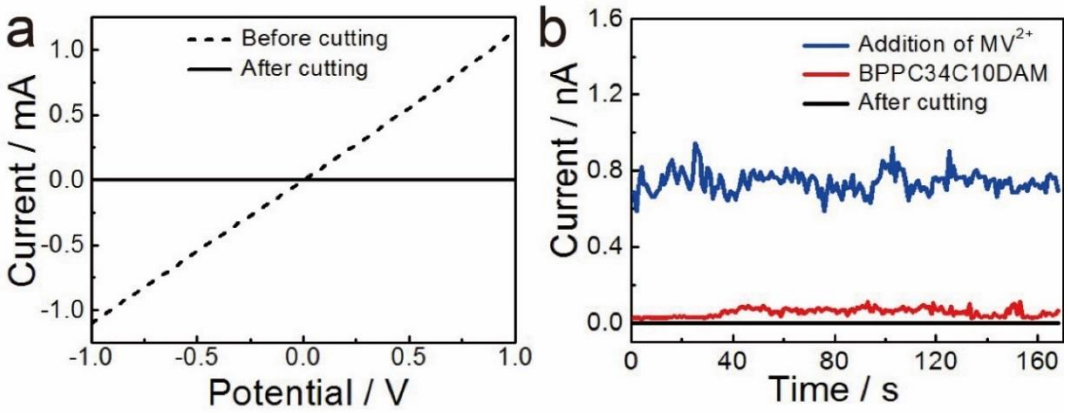

fig. S4. Solid-state electrical characterization. (**a**) *I-V* curves of a graphene device before (dash) and after (solid) e-beam lithographic cutting. (**b**) *I-t* curves of a representative graphene device (V_{bias} = 100 mV) after e-beam lithographic cutting (black), BPP34C10DAM EDCI coupling connection (red), and further treatments with 1 mM $MV{\cdot}2PF_6$ (blue), respectively. All data were collected using the Agilent characterization system.

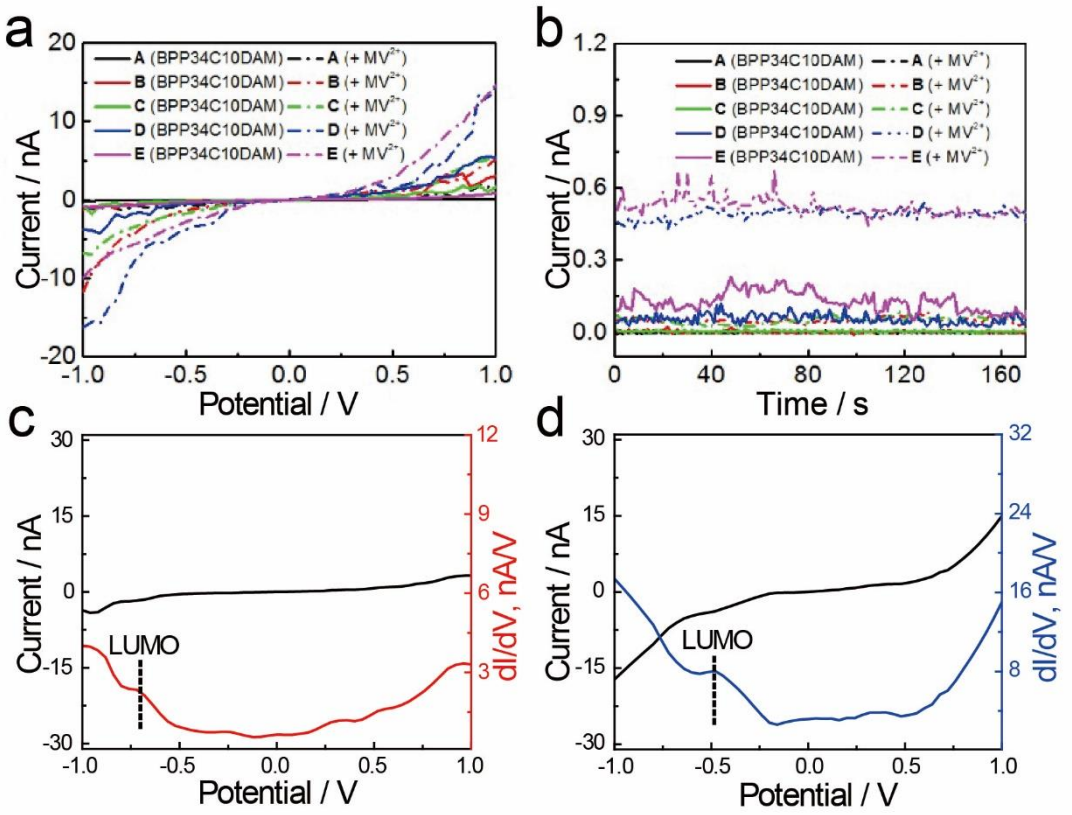

fig. S5. Reproducibility and differential conductance spectra. (**a**) *I-V* and (**b**) *I-t* curves measured using the Agilent characterization system on another five devices before and after MV·2PF$_6$ treatment, all showing the large enhancement of the current values after MV·2PF$_6$ addition (V_{bias} = 100 mV). (**c** and **d**) Representative *I-V* and d*I*/d*V* curves of BPP34C10 (c) and MV^{2+}⊂BPP34C10 (d) SMJ devices in the solid state at room temperature.

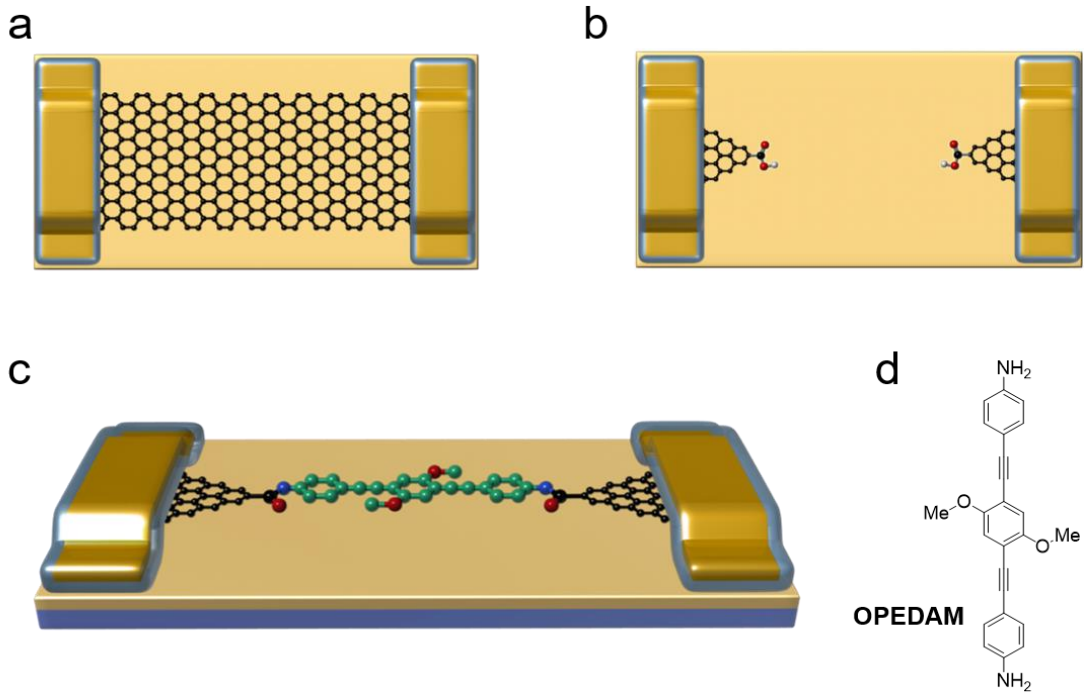

fig. S6. Schematic processes used to fabricate molecular devices. (**a**) Schematic representations of a pristine graphene device transferred from the PMMA support. (**b**) A graphene-based point contact device prepared using the dash line lithographic process and oxygen plasma etching. (**c**) OPEDAM-connected graphene device and (**d**) structural formula of OPEDAM.

5. The Single Molecule-Connection Analyses

The single molecule-connection process was carried out using EDCI coupling reactions to form amide bonds between COOH groups on the ends of graphene point contacts and amino groups at the termini of BPP34C10DAM backbones. The optimized connection yield ($Y_{\text{connection}}$), which is the fraction of the graphene point contact devices that showed increased current after EDCI coupling, were found to be 25% for BPP34C10DAM and 30% for OPEDAM under optimized conditions. Referring to previously reported results (*32*, *33*), the number of junctions that contribute to charge transport can be carried out by calculating the probability of the connected devices with *n*-rejoined junctions (G_n) with the binomial distribution and the optimized connection yields

$$G_n = \frac{m!}{n!\,(m-n)!} p^n (1-p)^{m-n} \qquad n = 0, 1, 2 \cdots, m$$

$$Y_{\text{connection}} = 1 - G_0 = 1 - \frac{m!}{0!\,(m-0)!} p^0 (1-p)^m$$

where m is the number of graphene point contact pairs (210 in the current case), p is the probability of successful connection for a random junction, and G_0 is the probability of devices without any connected junctions.

Using the $Y_{connection}$ values obtained, we can calculate the p values and the fractions $[G_n/(1–G_0)]$ of single-molecule-junctions (86% for BPP34C10DAM and 83% for OPEDAM) and two-molecule-junctions (12% for BPP34C10DAM and 15% for OPEDAM) in all successfully connected devices. These results from calculations suggest that, in most cases, charge transport in these devices is arising mainly in a single-molecule junction.

6. Characterization of Control Devices

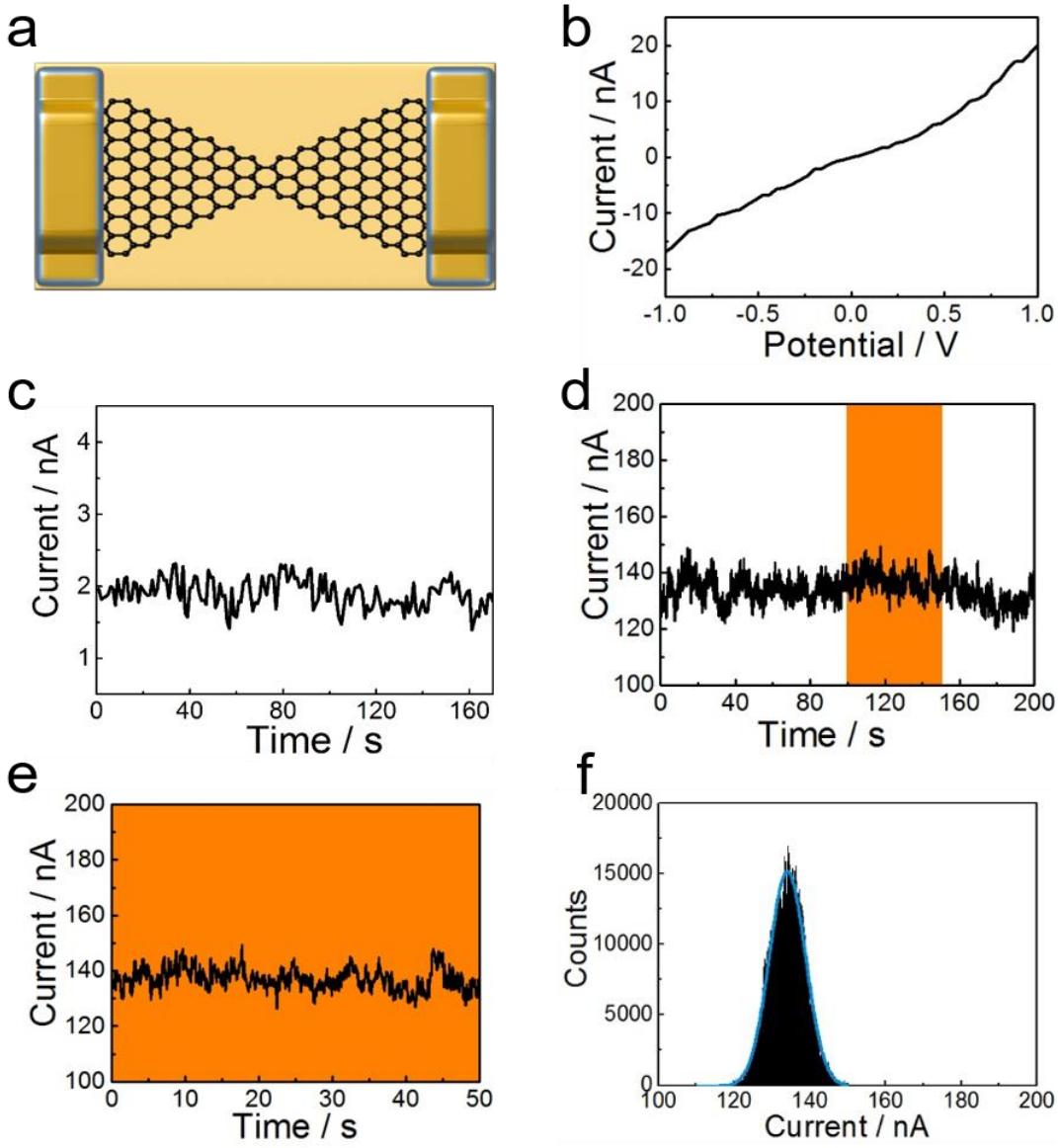

fig. S7. Control experiments using a partially cleaved graphene ribbon device. (**a**) Schematic representation of the partially cleaved graphene ribbon device. (**b**) *I-V* and (**c**) *I-t* curves of the control device in the solid state. (**d**) *I-t* curve of the control device immersed in Me_2SO solution of 1 mM $MV{\cdot}2PF_6$ at room temperature for 200 s. (**e**) Partial *I-t* curve of (D) (100~150 s). (**f**) The histogram of (e), showing a normal current distribution. V_{bias}= 100 mV.

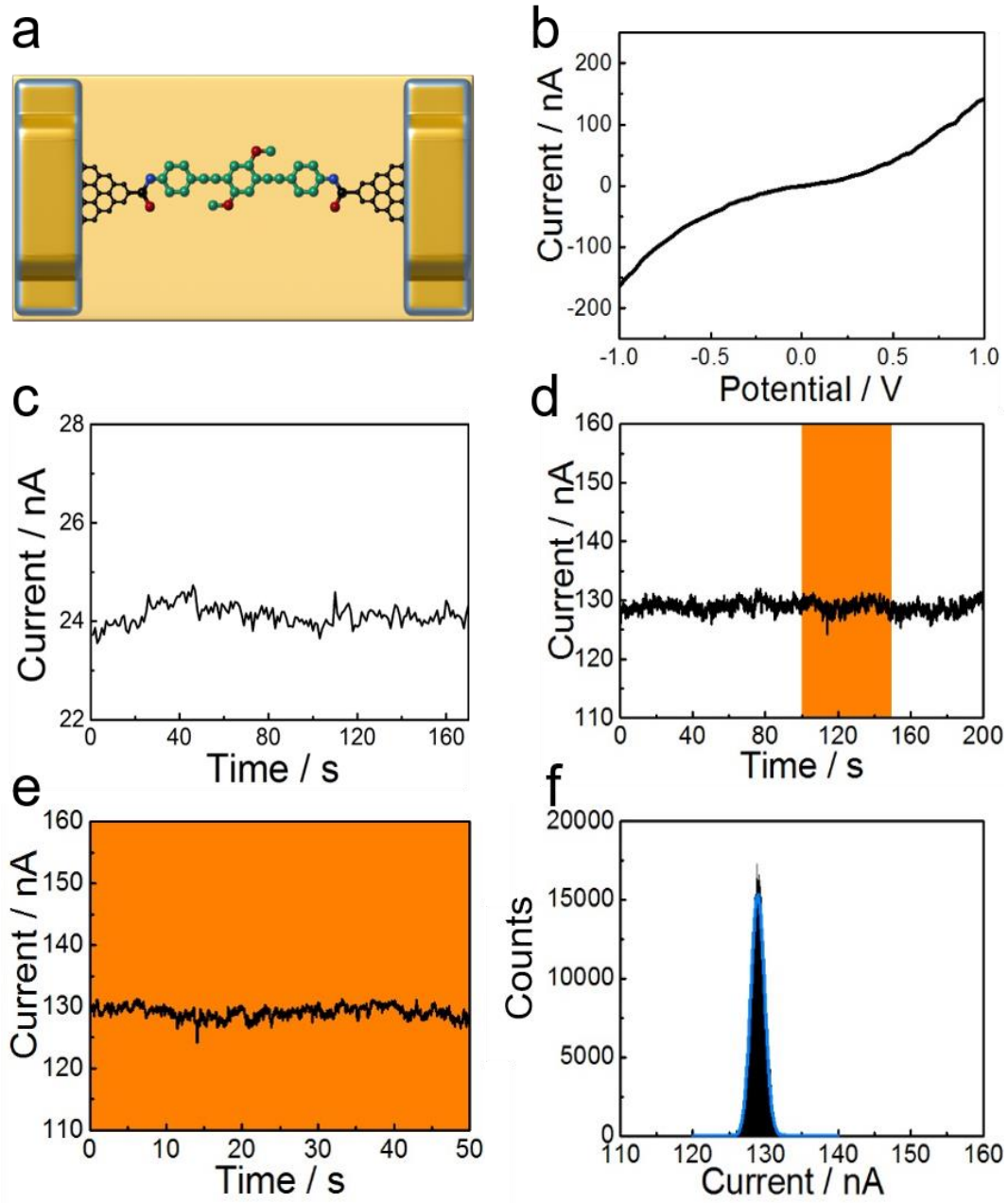

fig. S8. Control experiments using an OPEDAM-connected device. (**a**) Schematic representation of the OPEDAM-connected control device. (**b**) *I-V* and (**c**) *I-t* curves of the control device in the solid state. (**d**) *I-t* curve of the control device immersed in Me_2SO solution of 1 mM $MV{\cdot}2PF_6$ at room temperature for 200 s. (**e**) Partial *I-t* curve of (D) (100~150 s). (**f**) The histogram of (e), showing a normal current distribution. V_{bias} = 100 mV.

7. Real-Time Measurements of SMJs at the Device-Liquid Interface

Illustrated in figs. S9 to S12, an additional SMJ device-liquid interface characterization device was set up for real-time measurements (the same mode as that of Fig. 4), revealing similar results to those shown in Fig. 4.

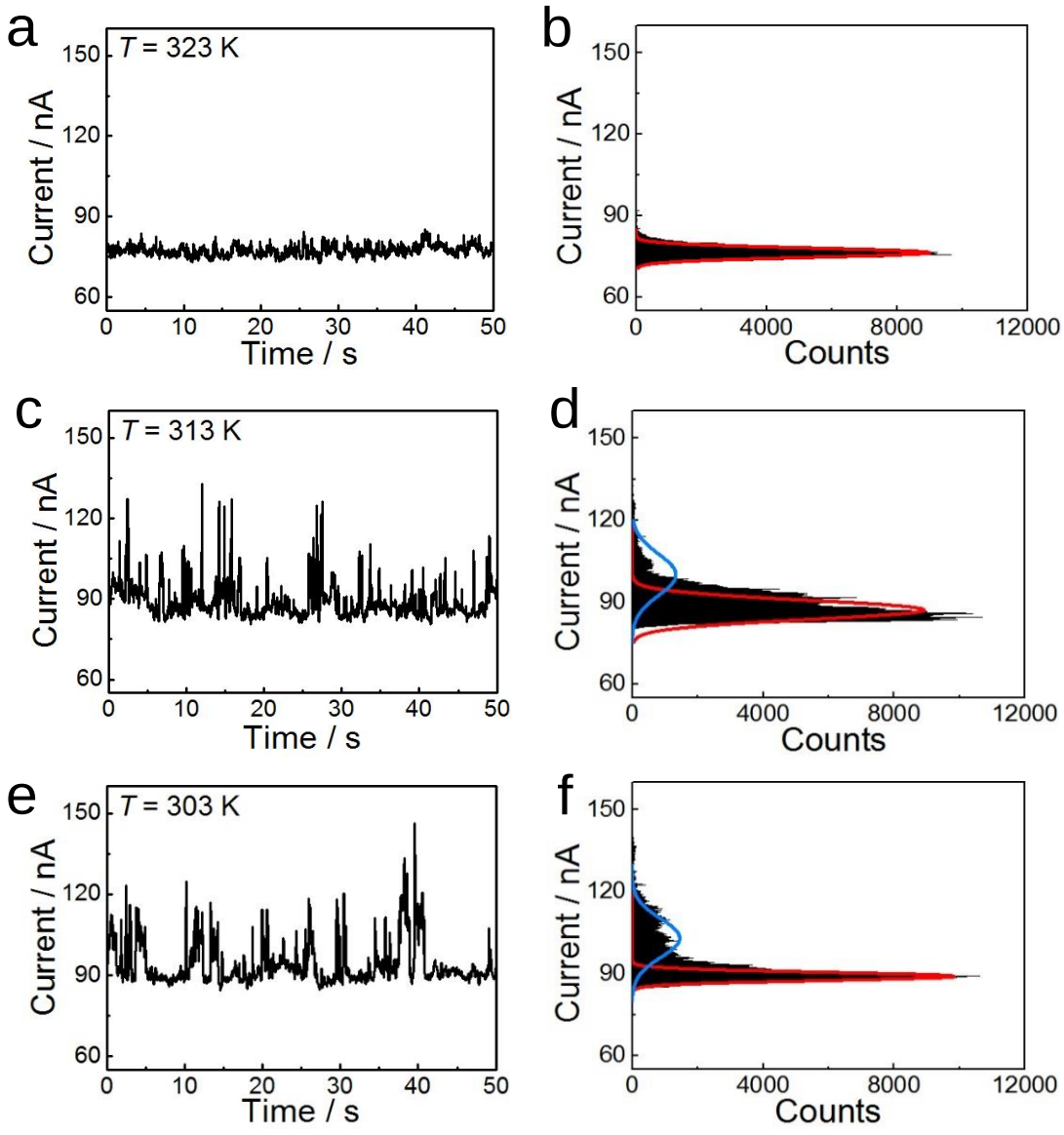

fig. S9. Real-time measurements of host-guest dynamics in SMJs at the device-liquid interface. (**a**, **c**, **e**) *I-t* curves and (**b**, **d**, **f**) the corresponding histograms of a MV^{2+}⊂BPP34C10-SMJ device merged with 1 mM $MV{\cdot}2PF_6$ Me_2SO solution at three different temperatures (323, 313, and 303 K, from top to bottom) with a 28.8 kSa/s sampling rate. V_{bias} = 100 mV.

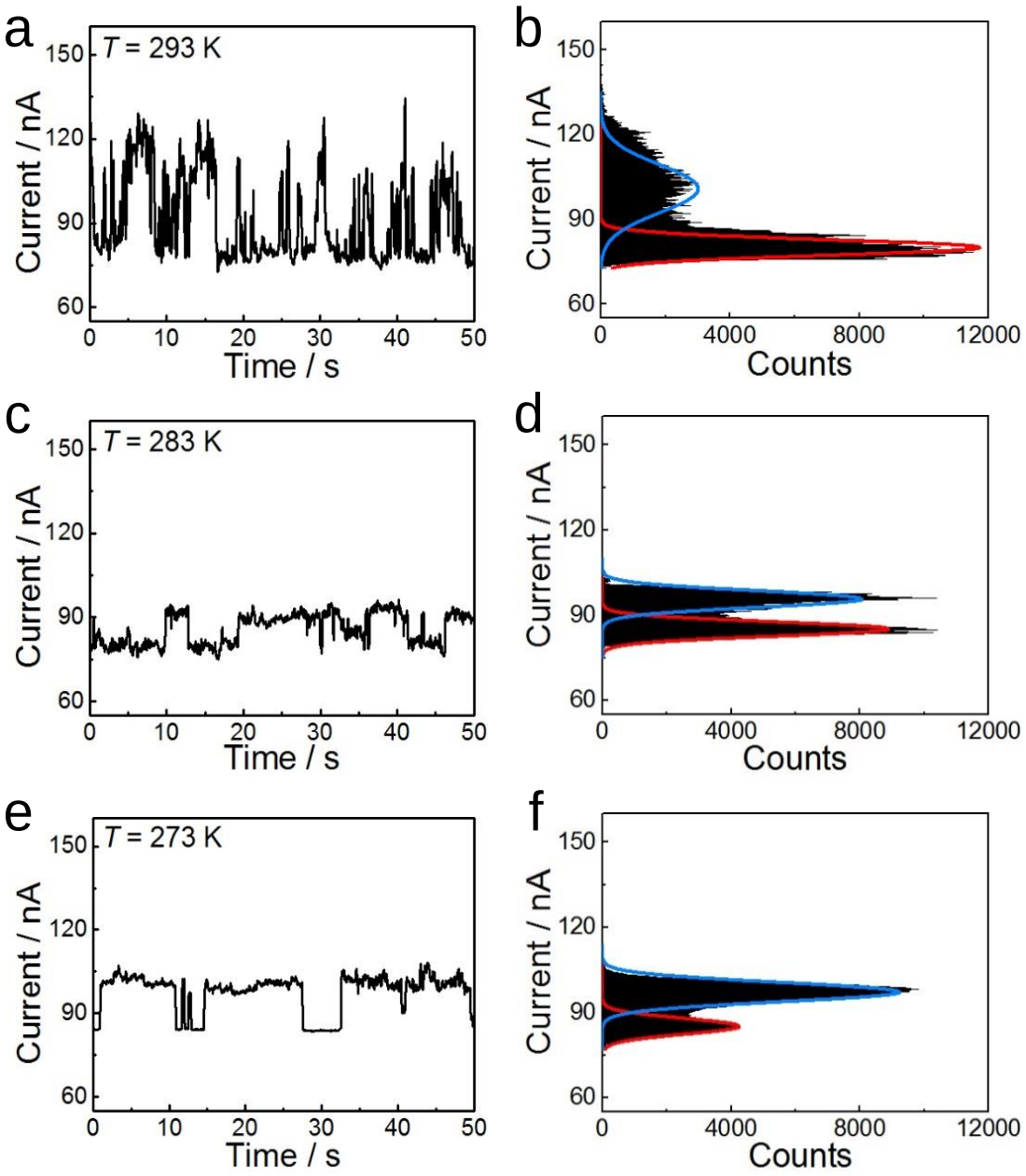

fig. S10. Real-time measurements of host-guest dynamics in SMJs at the device-liquid interface. (**a**, **c**, **e**) *I-t* curves and (**b**, **d**, **f**) the corresponding histograms of a MV^{2+}⊂BPP34C10-SMJ device merged with 1 mM $MV{\cdot}2PF_6$ Me_2SO solution at three different temperatures (293, 283, and 273 K, from top to bottom) with a 28.8 kSa/s sampling rate. V_{bias} = 100 mV.

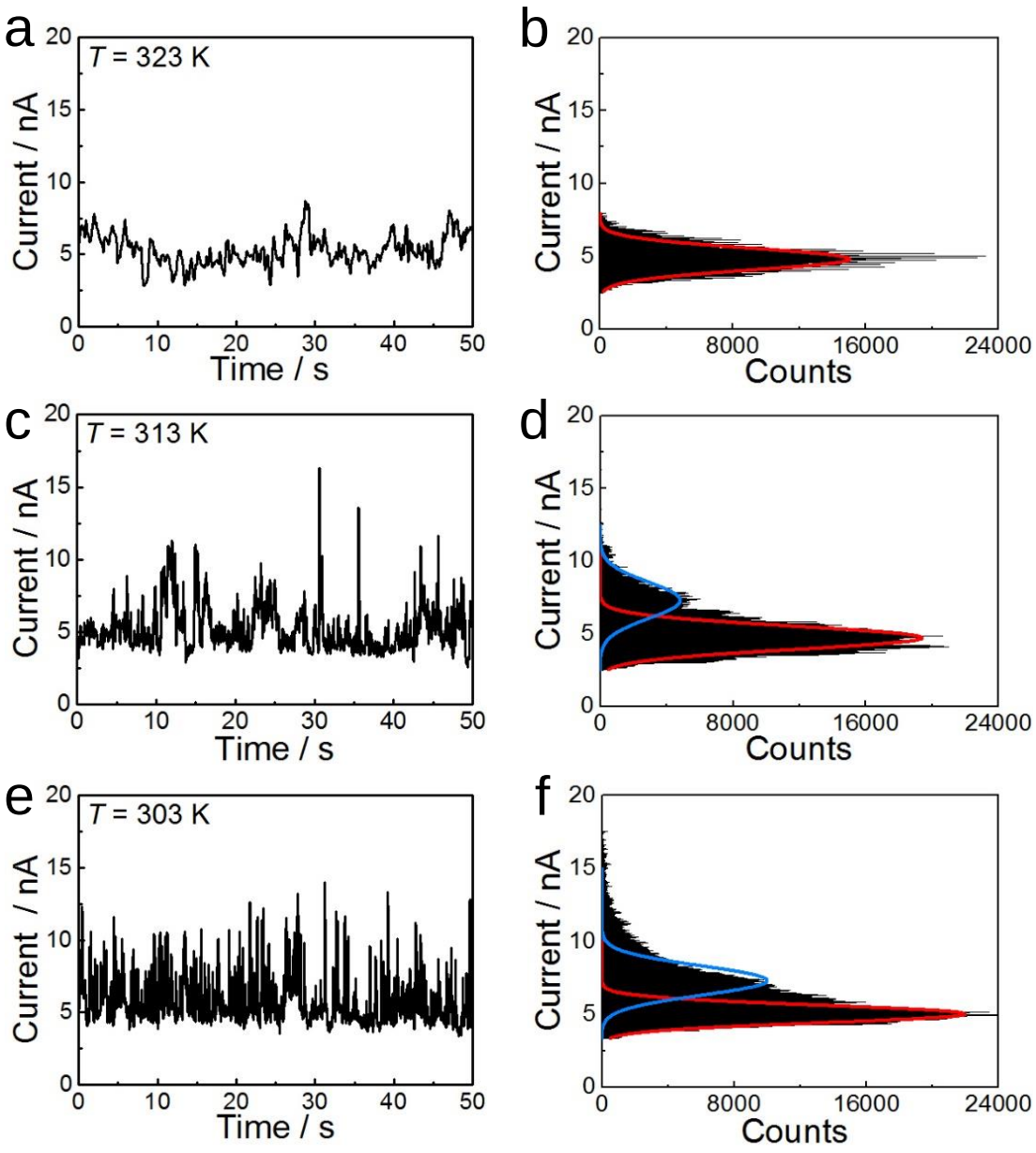

fig. S11. Real-time measurements of host-guest dynamics in SMJs at the device-liquid interface. (**a**, **c**, **e**) *I-t* curves and (**b**, **d**, **f**) the corresponding histograms of a MV^{2+}⊂BPP34C10-SMJ device merged with 1 mM MV·2Cl aqueous solution at three different temperatures (323, 313, and 303 K, from top to bottom) with a 28.8 kSa/s sampling rate. V_{bias} = 100 mV.

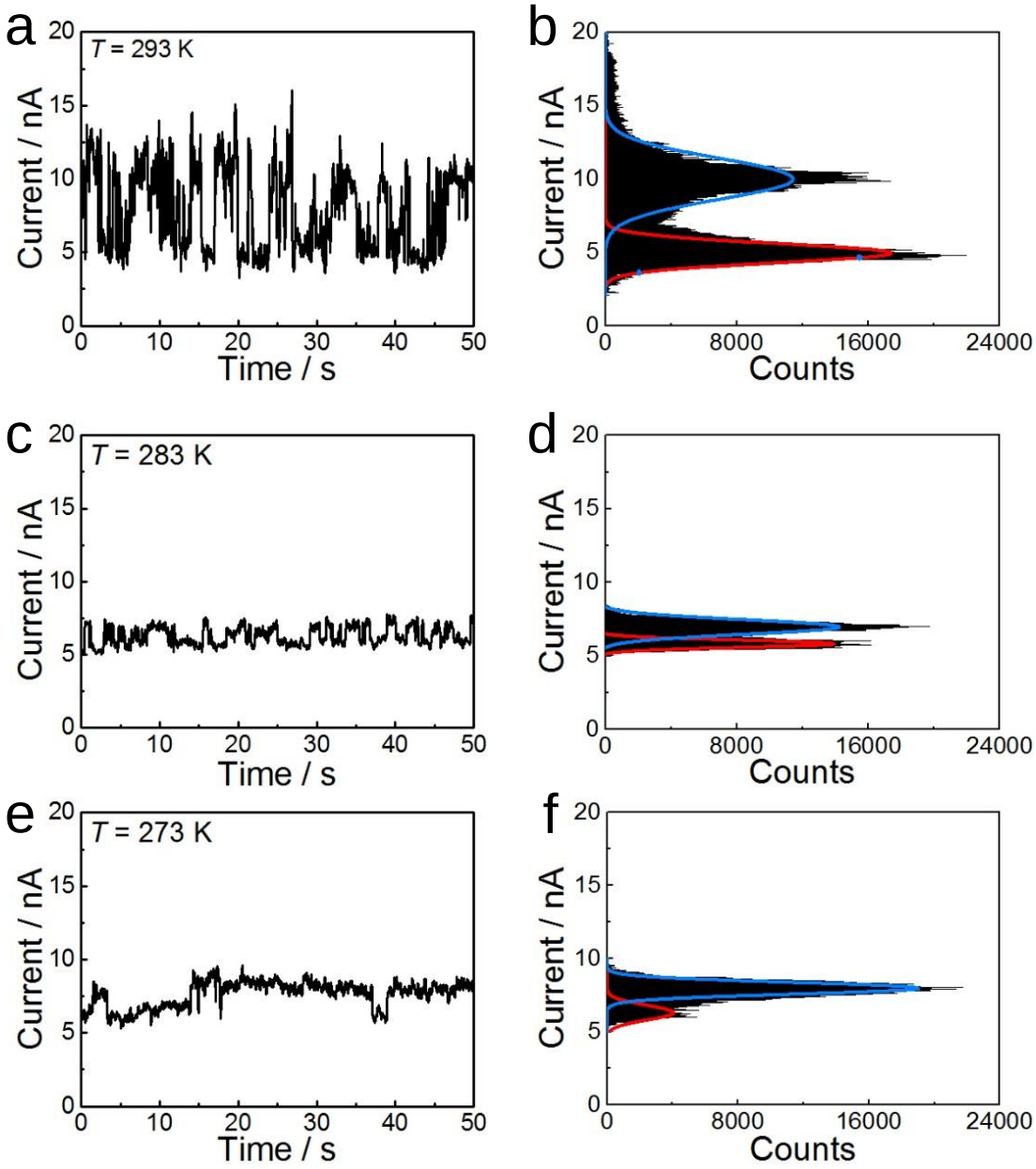

fig. S12. Real-time measurements of host-guest dynamics in SMJs at the device-liquid interface. (**a**, **c**, **e**) *I-t* curves and (**b**, **d**, **f**) the corresponding histograms of a MV^{2+}⊂BPP34C10-SMJ device merged with 1 mM MV·2Cl aqueous solution at three different temperatures (293, 283, and 273 K, from top to bottom) with a 28.8 kSa/s sampling rate. V_{bias} = 100 mV.

8. Thermodynamic Analyses: Binding Constants

Binding constants between BPP34C10 and MV^{2+} for five different devices in Me_2SO and in aqueous solution were obtained and summarized in the tables S1 to S6.

table S1. Binding constants. Binding constants (K_a, M^{-1}) between BPP34C10 and MV·2PF_6 / MV·2Cl from time interval results of the first device at five different temperatures (313, 303, 293, 283, and 273 K) in Me_2SO or aqueous solution, respectively.

T (K)	A_{low} (Me_2SO)	A_{high} (Me_2SO)	K_a (Me_2SO)	A_{low} (H_2O)	A_{high} (H_2O)	K_a (H_2O)
323	97840.5	N/A	N/A	22694.8	N/A	N/A
313	69602.0	17045.0	250	23333.0	6089.7	267
303	51426.9	44703.0	887	15751.0	14895.4	961
293	79498.1	74316.7	923	21121.2	34187.5	1632
283	54258.7	80220.8	1500	7313.9	14657.8	2030
273	12537.4	49711.6	4000	2249.0	12990.5	5667

table S2. Binding constants. Binding constants (K_a, M^{-1}) between BPP34C10 and MV·2PF_6 / MV·2Cl from time interval results of the second device at five different temperatures (313, 303, 293, 283, and 273 K) in Me_2SO or aqueous solution, respectively.

T (K)	A_{low} (Me_2SO)	A_{high} (Me_2SO)	K_a (Me_2SO)	A_{low} (H_2O)	A_{high} (H_2O)	K_a (H_2O)
323	38361.2	N/A	N/A	28276.2	N/A	N/A
313	78311.0	25203.1	316	38875.8	15108.8	389
303	37006.2	25517.5	695	33060.9	25064.5	754
293	80821.7	64129.4	786	28346.7	40066.1	1439
283	55997.5	58388.3	1041	8885.7	18205.3	2030
273	10413.4	50725.0	4882	5131.5	28395.5	5667

table S3. Binding constants. Binding constants (K_a, M^{-1}) between BPP34C10 and MV·2PF_6 / MV·2Cl from time interval results of the third device at five different temperatures (313, 303, 293, 283, and 273 K) in Me_2SO or aqueous solution, respectively.

T (K)	A_{low} (Me_2SO)	A_{high} (Me_2SO)	K_a (Me_2SO)	A_{low} (H_2O)	A_{high} (H_2O)	K_a (H_2O)
323	55467.6	N/A	N/A	59754.8	N/A	N/A
313	89583.4	38551.5	429	23970.4	11613.2	493
303	73292.3	47357.8	639	43165.5	35602.7	818
293	94416.8	74221.5	786	8826.8	15060.0	1703
283	33056.5	51027.1	1564	9380.4	29652.0	3042
273	33056.8	86421.3	2571	5090.2	19067.6	3762

table S4. Binding constants. Binding constants (K_a, M^{-1}) between BPP34C10 and MV·2PF_6 / MV·2Cl from time interval results of the forth device at five different temperatures (313, 303, 293, 283, and 273 K) in Me_2SO or aqueous solution, respectively.

T (K)	A_{low} (Me_2SO)	A_{high} (Me_2SO)	K_a (Me_2SO)	A_{low} (H_2O)	A_{high} (H_2O)	K_a (H_2O)
323	71990.7	N/A	N/A	27581.3	N/A	N/A
313	77843.5	34835.4	449	14442.8	5268.8	370
303	45997.1	31872.6	695	7519.9	7070.0	941
293	35308.2	31683.1	887	29086.0	50309.1	1703
283	37412.2	92579.4	2448	6479.1	22095.3	3348
273	28101.1	93894.8	3348	3328.4	19048.6	5667

table S5. Binding constants. Binding constants (K_a, M^{-1}) between BPP34C10 and MV·2PF_6 / MV·2Cl from time interval results of the fifth device at five different temperatures (313, 303, 293, 283, and 273 K) in Me_2SO or aqueous solution, respectively.

T (K)	A_{low} (Me_2SO)	A_{high} (Me_2SO)	K_a (Me_2SO)	A_{low} (H_2O)	A_{high} (H_2O)	K_a (H_2O)
323	101083.0	N/A	N/A	44684.0	N/A	N/A
313	115658.1	37398.7	316	31731.3	10371.8	333
303	78183.3	52557.3	667	11530.6	9559.8	818
293	95608.0	83727.6	887	24562.6	33254.4	1381
283	42090.5	74113.4	1778	17783.8	38632.6	2125
273	29335.7	77675.5	2704	4257.8	13327.9	3167

table S6. Binding constants. Binding constants (K_a, M^{-1}) between BPP34C10 and MV·2PF_6 / MV·2Cl for the results of mean (M) and standard deviation (SD) from all of the above patches of time intervals at five different temperatures (313, 303, 293, 283, and 273 K) in Me_2SO or aqueous solution, respectively.

T (K)	323	313	303	293	283	273
K_a (M, Me_2SO)	N/A	352	717	854	1666	3501
SD (Me_2SO)	N/A	84	98	64	513	959
K_a (M, H_2O)	N/A	370	858	1572	2515	4786
SD (H_2O)	N/A	83	89	152	631	1225

9. Thermodynamic Analyses of SMJ Devices

Assuming a two-state model where BPP34C10 is either free or complexed in the SMJ system, the association equilibrium constant K_a can be presented (fig. S13) as the Langmuir isotherm $K_a = \alpha/(1-\alpha)C$, where α is the fraction of the complexed state between MV^{2+} and BPP34C10 in the total host concentration, and C is the concentration of added MV^{2+} dications

For other thermodynamic parameters (*39*) (eqs. S1-S3)

$$\Delta G^0 = -RT \cdot \ln Ka \quad \text{(S1)}$$

$$\Delta G^0 = \Delta H^0 - T\Delta S^0 \quad \text{(S2)}$$

$$-\ln Ka = \frac{\Delta H^0}{R \cdot T} - \Delta S^0 \quad \text{(S3)}$$

ΔG^o is derived from the K_a value while ΔH^o and ΔS^o are obtained by a linear fitting of eq. S3.

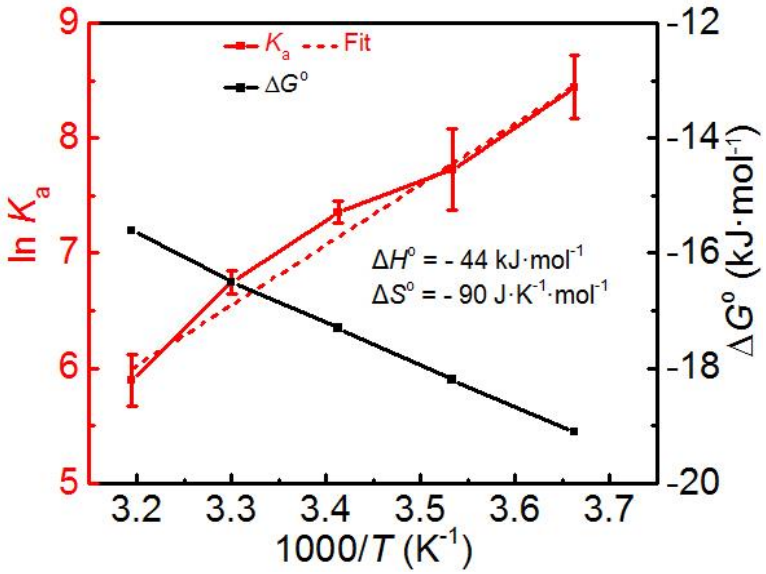

fig. S13. Thermodynamic analyses of SMJ devices. Plots of the thermodynamic parameters (lnK_a *vs.* 1000/*T*, ΔG^o *vs.* 1000/*T*) deduced from single-molecule measurements at the SMJ device-H_2O interface with 1 mM MV·2Cl at 293 K. Error bars were calculated from the data obtained from five different devices. ΔH^o and ΔS^o were obtained by using the van't Hoff equation, $-RT\ln(K_a) = \Delta H^o - T\Delta S^o$.

10. ^{1}H-NMR Titrations and Analyses

^{1}H-NMR titration tests were performed with Bruker Advanced 600 MHz in CD_3SOCD_3 and D_2O solution. As shown in fig. S14, BPP34C10DA was treated as a host with a constant concentration of 6.1 mM, while the concentration of methyl viologen (guest) was allowed to range from 0.3 to 70 times of host concentration. The titration tests were carried out at four different temperatures from 293 to 323 K.

The chemical shift (δ, ppm) data were collected with a Bruker Avance III 600 MHz spectrometer at four different temperatures from 293 to 323 K, and are listed in tables S7 and S8.

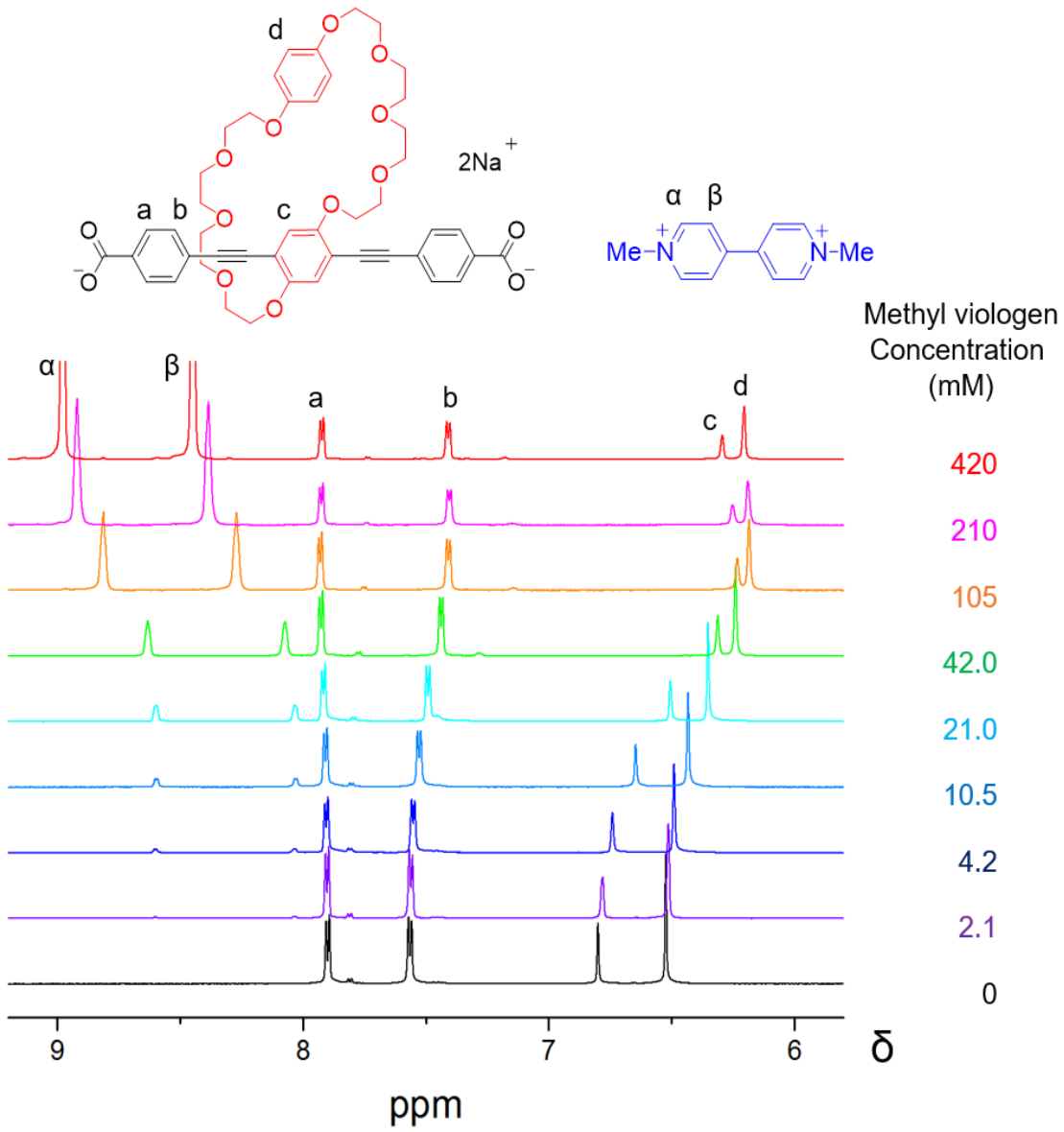

fig. S14. ^{1}H NMR titration. Plots of ^{1}H-NMR spectra from titrations of BPP34C10DA·2Na (host) and MV·2Cl (guest) in D_2O at 293 K (c_{host}= 6.1 mM, c_{guest}= 2.1~ 420 mM).

table S7. Chemical shifts for 1H NMR titrations in CD_3SOCD_3. Chemical shift (δ, ppm) obtained from CD_3SOCD_3 solution of BPP34C10DA and MV·2PF_6. c and d are the peaks labeled in fig. S14.

Host concentration mM	Guest concentration mM	δ (ppm) 293 K		δ (ppm) 303 K		δ (ppm) 313 K		δ (ppm) 323 K	
		c	d	c	d	c	d	c	d
6.062	420.16	6.71	6.24	6.75	6.28	6.81	6.34	6.89	6.40
6.062	210.08	6.77	6.29	6.85	6.36	6.94	6.44	7.00	6.49
6.062	105.05	6.90	6.39	6.99	6.47	7.06	6.54	7.11	6.59
6.062	42.03	7.00	6.48	7.10	6.56	7.14	6.60	7.16	6.63
6.062	21.01	7.10	6.56	7.14	6.6	7.17	6.63	7.18	6.64
6.062	10.5	7.15	6.59	7.18	6.62	7.19	6.64	7.2	6.66
6.062	4.2	7.20	6.63	7.21	6.65	7.21	6.66	7.21	6.67
6.062	2.1	7.22	6.65	7.22	6.66	7.22	6.66	7.22	6.67
6.062	1.05	7.23	6.66	7.22	6.66	7.22	6.67	7.22	6.67
6.062	0	7.24	6.66	7.23	6.67	7.23	6.67	7.22	6.68

table S8. Chemical shifts for 1H NMR titrations in D_2O. Chemical shift (δ, ppm) obtained from D_2O solution of BPP34C10DA sodium salt and MV·2Cl. c and d are the peaks labeled in fig. S14.

Host concentration mM	Guest concentration mM	δ (ppm) 293 K		δ (ppm) 303 K		δ (ppm) 313 K		δ (ppm) 323 K	
		c	d	c	d	c	d	c	d
6.062	420.16	6.20	6.12	6.85	6.57	6.96	6.69	7.10	6.81
6.062	210.08	6.16	6.10	6.83	6.56	6.96	6.68	7.09	6.80
6.062	105.05	6.14	6.10	6.79	6.53	6.93	6.66	7.06	6.78
6.062	42.03	6.22	6.15	6.70	6.48	6.85	6.61	7.00	6.75
6.062	21.01	6.42	6.26	6.57	6.41	6.74	6.55	6.90	6.69
6.062	10.5	6.56	6.34	6.41	6.30	6.59	6.46	6.79	6.61
6.062	4.2	6.65	6.40	6.31	6.24	6.49	6.39	6.68	6.54
6.062	2.1	6.69	6.42	6.32	6.24	6.50	6.39	6.68	6.53
6.062	1.05	6.71	6.43	6.85	6.57	6.96	6.69	7.10	6.81

For a classic calculation (eqs. S4-S11) of binding constants from ^{1}H-NMR titration data, refer to a review of Hirose (*36*). The procedure is shown as follows for a 1:1 complex in this case

$$H + G \leftrightarrow C \tag{S4}$$

$$K = \frac{[C]}{[H]\cdot[G]} \tag{S5}$$

$$[H]_t = [H] + [C] \tag{S6}$$

$$[G]_t = [G] + [C] \tag{S7}$$

$$K = \frac{[C]}{([H]_t - [C])([G]_t - [C])} \tag{S8}$$

$$\delta = \delta_h \cdot (1 - x) + \delta_c\,, \text{ where } x = \frac{[C]}{[H]_t} \tag{S9}$$

$$[H]_t \cdot (\delta - \delta_h) = [C] \cdot (\delta_c - \delta_h) \tag{S10}$$

Set $K = y$, by combining eqs. S8-S10 we can deduce that

$$y = \frac{x}{(1-x)\cdot([G]_t - [H]_t \cdot x)} \tag{S11}$$

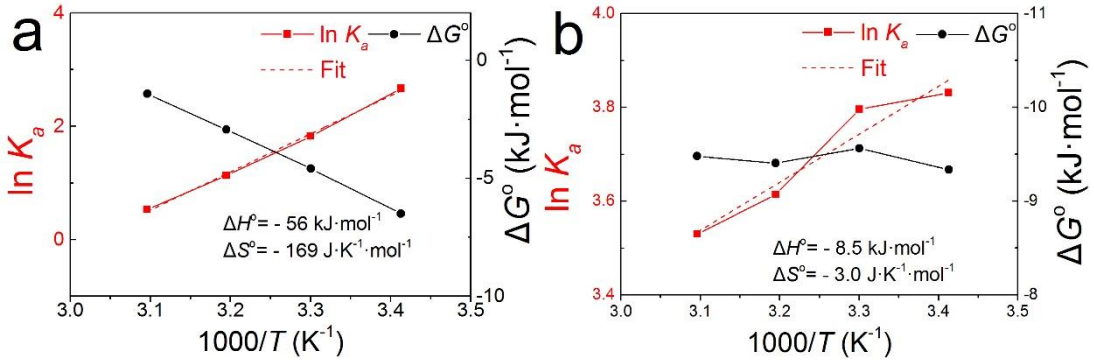

fig. S15. Thermodynamic analyses of SMJ devices. Plots of the thermodynamic parameters (lnK_a *vs.* 1000/*T*, ΔG^o *vs.* 1000/*T*) deduced from ^{1}H-NMR measurements for BPP34C10 with 1 mM MV^{2+} at different temperatures in solution of (**a**) CD_3SOCD_3 and (**b**) D_2O. ΔH^o and ΔS^o were obtained by using the van't Hoff equation, $-RT\ln(K_a) = \Delta H^o - T\Delta S^o$.

11. Kinetic Analyses of SMJ Devices

To further study the relationships between the "high" and "low" conductance states and molecular interactions in MV^{2+}⊂BPP34C10-SMJ, the *I-t* data was first processed by using a QUB software. This idealized two-level flip-flops were further analysed to provide one set of kinetic parameters of the MV^{2+}⊂BPP34C10-SMJ devices, including the lifetimes τ_{high} and τ_{low}.

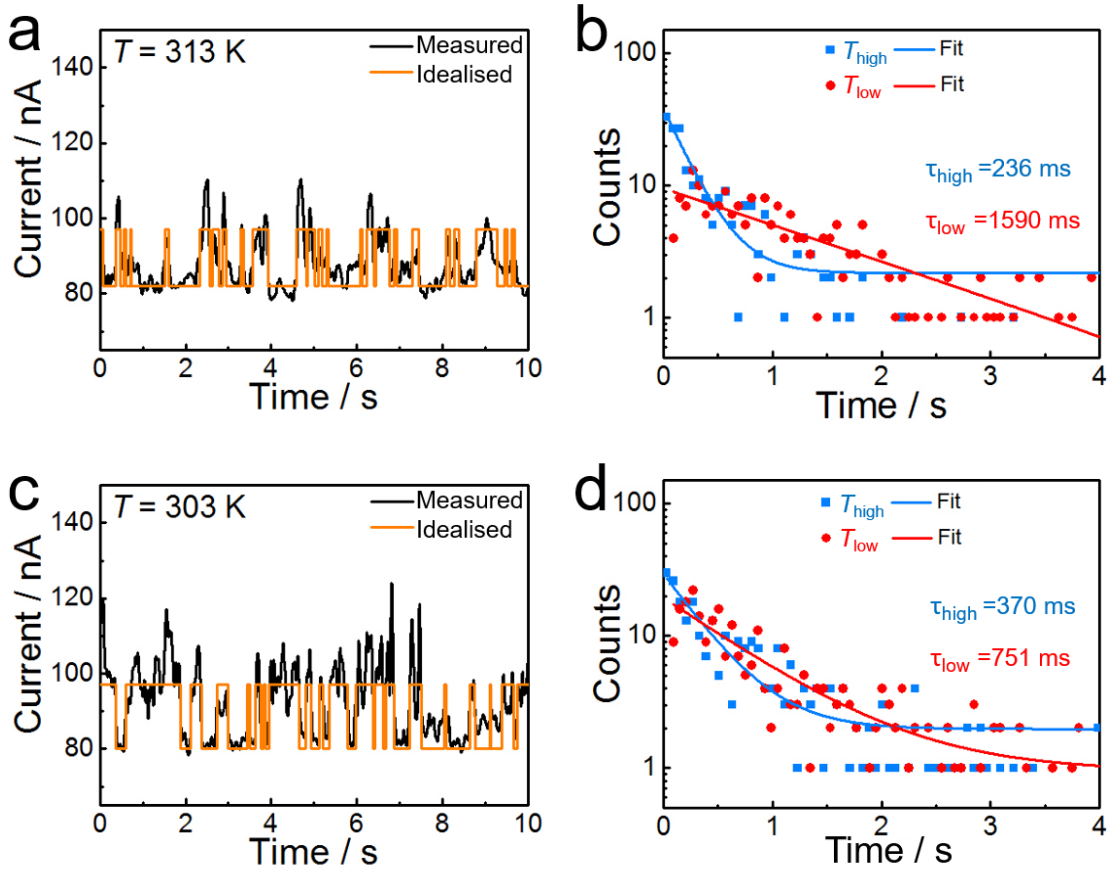

fig. S16. Host-guest kinetics analysis. (**a**) and (**c**) *I-t* curves (black) of a BPP34C10-SMJ device in Me_2SO solution of 1 mM MV·$2PF_6$ at different temperatures (313 and 303 K, from top to bottom), and the idealized fitting (orange) obtained from a segmental *k*-means (SKM) method based on a hidden-Markov-model analysis using a QUB software. V_{bias} = 100 mV. (**b**) and (**d**) Plots of time-intervals of the "high" (T_{high}, blue) and "low" (T_{low}, red) current states in the idealized fitting in (a) and (c), and their exponential fittings in which the lifetimes of two states (τ_{high} and τ_{low}) can be derived.

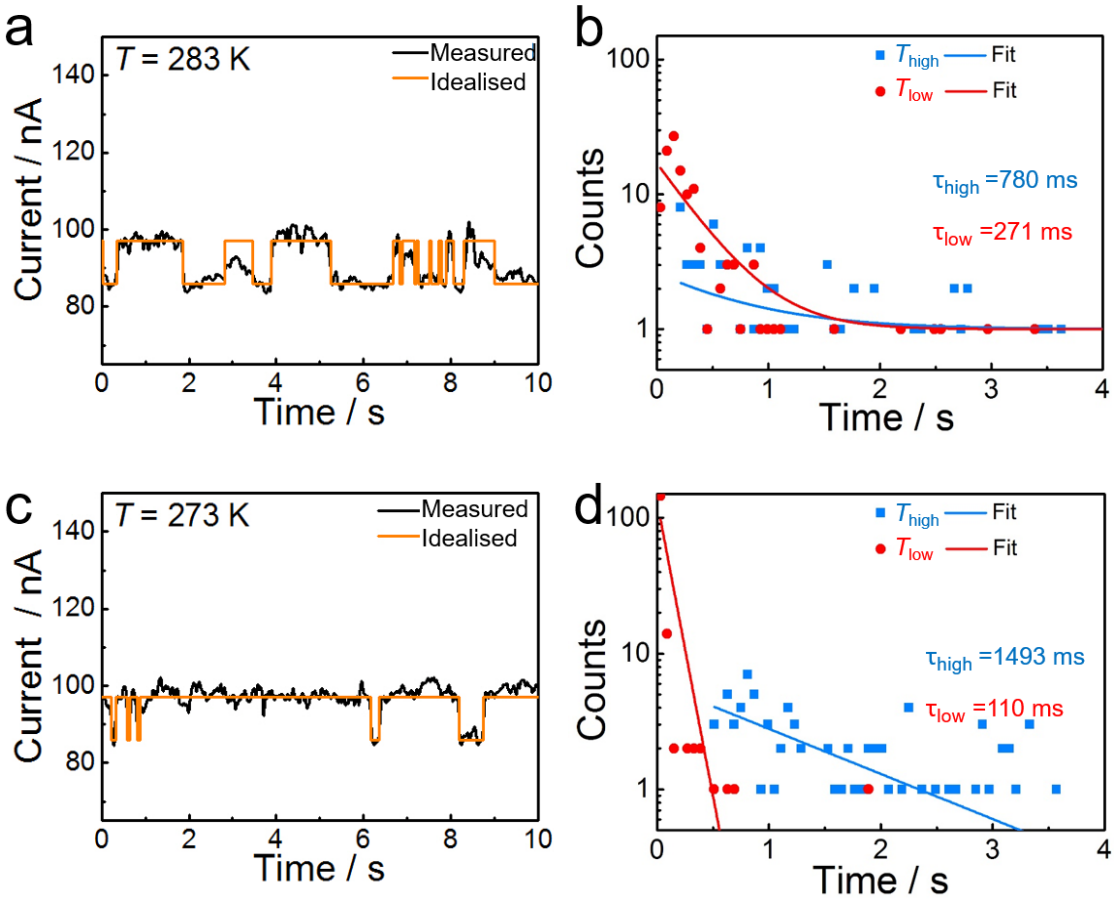

fig. S17. Host-guest kinetics analysis. (**a**) and (**c**) *I-t* curves (black) of a BPP34C10-SMJ device in Me_2SO solution of 1 mM MV·2PF_6 at different temperatures (283 and 273 K, from top to bottom), and the idealized fitting (orange) obtained from a segmental *k*-means (SKM) method based on a hidden-Markov-model analysis using a QUB software. V_{bias} = 100 mV. (**b**) and (**d**) Plots of time-intervals of the "high" (T_{high}, blue) and "low" (T_{low}, red) current states in the idealized fitting in (a) and (c), and their exponential fittings in which the lifetimes of two states (τ_{high} and τ_{low}) can be derived.

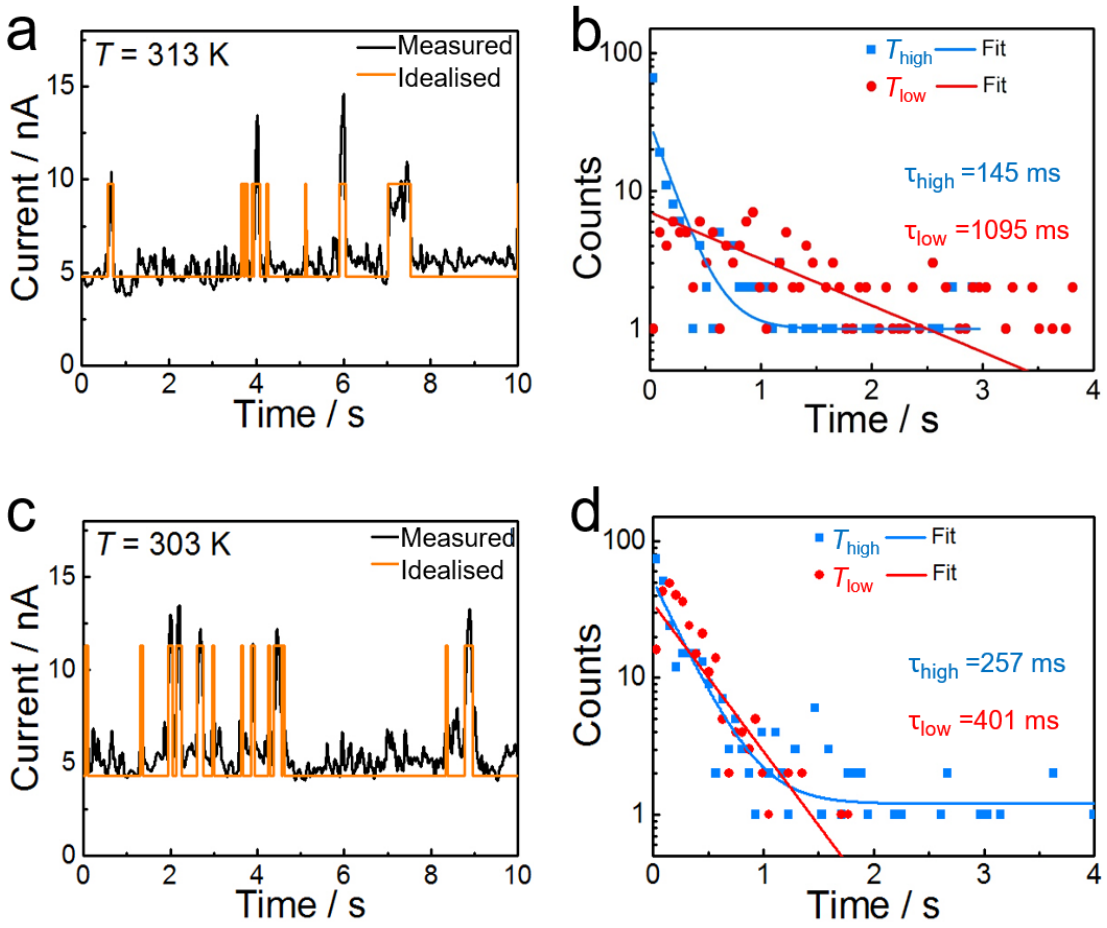

fig. S18. Host-guest kinetics analysis. (**a**) and (**c**) *I-t* curves (black) of a BPP34C10-SMJ device in aqueous solution of 1 mM MV·2Cl at different temperatures (313 and 303 K, from top to bottom), and the idealized fitting (orange) obtained from a segmental *k*-means (SKM) method based on a hidden-Markov-model analysis using a QUB software. V_{bias} = 100 mV. (**b**) and (**d**) Plots of time-intervals of the "high" (T_{high}, blue) and "low" (T_{low}, red) current states in the idealized fitting in (a) and (c), and their exponential fittings in which the lifetimes of two states (τ_{high} and τ_{low}) can be derived.

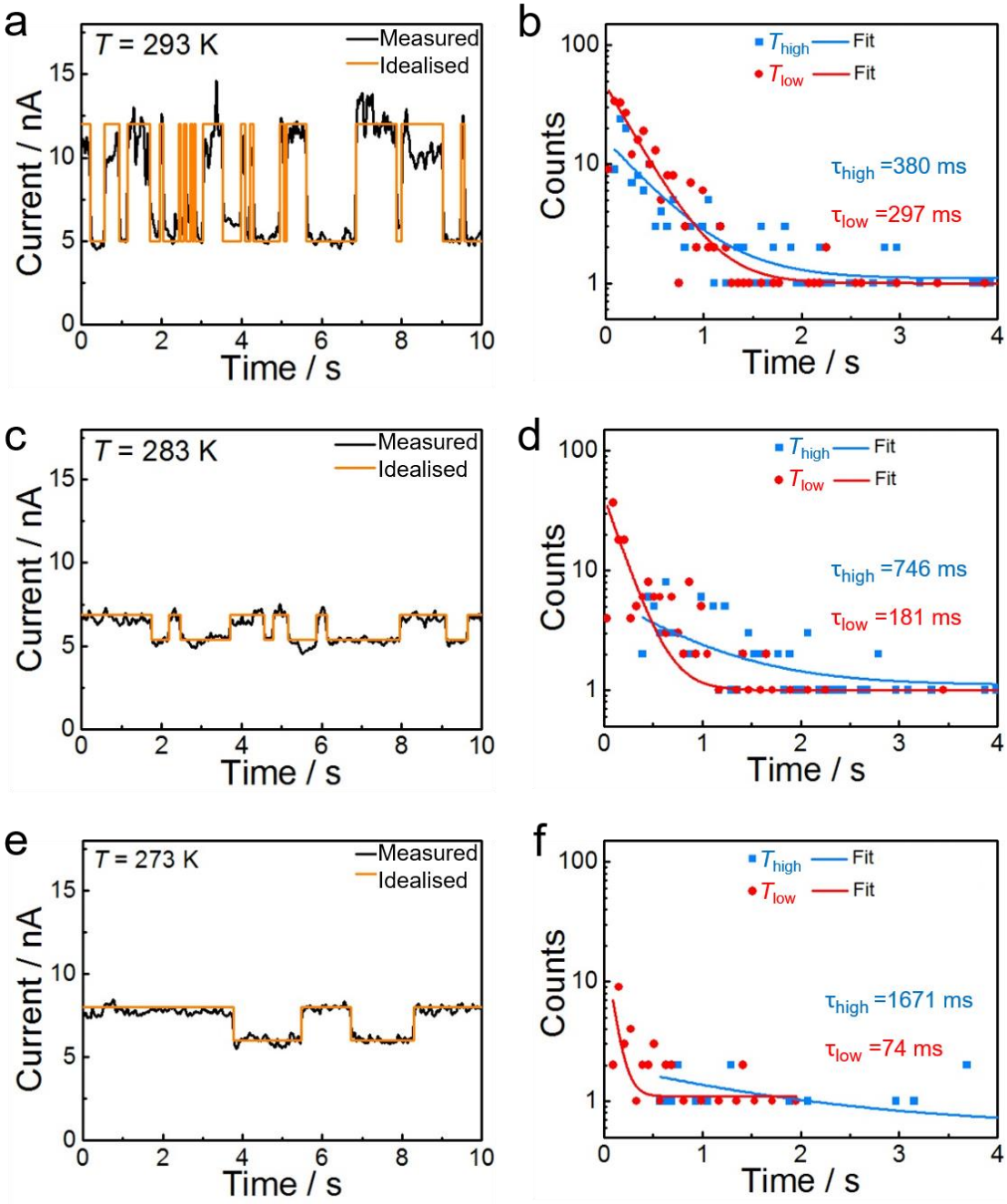

fig. S19. Host-guest kinetics analysis. (**a**, **c**, **e**) *I-t* curves (black) of a BPP34C10-SMJ device in aqueous solution of 1 mM MV·2Cl at different temperatures (293-273 K, from top to bottom), and the idealized fitting (orange) obtained from a segmental *k*-means (SKM) method based on a hidden-Markov-model analysis using a QUB software. V_{bias} = 100 mV. (**b**, **d**, **f**) Plots of time-intervals of the "high" (T_{high}, blue) and "low" (T_{low}, red) current states in the idealized fitting in (a), (c) and (e), and their exponential fittings in which the lifetimes of two states (τ_{high} and τ_{low}) can be derived.

12. Kinetic Analyses: Association and Dissociation Rate Constants

Association and dissociation rates between BPP34C10 and $MV \cdot 2PF_6$ / $MV \cdot 2Cl$ for five devices in Me_2SO and aqueous solution were obtained and are summarized in tables S9 to S14 and fig. S20. The dwell time shows that most time-intervals in-between blocking events are at the subsecond level. Considering the structure of the SMJ device, in which a single BPP34C10DAM molecular wire is attached between the graphene point contacts as the charge transport pathway, the reversible on-site supramolecular (de)complexation processes are presumably first-order. In our measurement results, the "high" and "low" state time-intervals are best fitted as first-order decaying exponential, suggesting that both states are related to a first-order process in the MV^{2+}⊂BPP34C10-SMJ device.

table S9. Dissociation (k_d) and association (k_a) rate constants. Dissociation (k_d) and association rate constants (k_a) of pseudorotaxane MV^{2+}⊂BPP34C10 from time interval results of the first device at five different temperatures in Me_2SO and aqueous solutions, respectively. The dwell time of their "high" and "low" states (τ_{high} and τ_{low}) were also calculated.

T (K)	323	313	303	293	283	273
τ_{high} (Me_2SO, ms)	N/A	235.5	370.0	420.0	780.0	1492.9
τ_{low} (Me_2SO, ms)	N/A	1590.0	750.8	568.4	270.7	110.0
k_d (Me_2SO, s^{-1})	N/A	4.3	2.7	2.4	1.3	0.7
k_a (Me_2SO, s^{-1})	N/A	0.6	1.3	1.8	3.7	9.1
τ_{high} (H_2O, ms)	N/A	144.5	257.4	380.0	745.5	1670.9
τ_{low} (H_2O, ms)	N/A	1095.3	401.3	296.6	180.9	73.6
k_d (H_2O, s^{-1})	N/A	6.9	3.9	2.6	1.3	0.6
k_a (H_2O, s^{-1})	N/A	0.9	2.5	3.4	5.5	13.6

table S10. Dissociation (k_d) and association (k_a) rate constants. Dissociation (k_d) and association rate constants (k_a) of pseudorotaxane MV^{2+}⊂BPP34C10 from time interval results of the second device at five different temperatures in Me_2SO and aqueous solutions, respectively. The dwell time of their "high" and "low" states (τ_{high} and τ_{low}) were also calculated.

T (K)	323	313	303	293	283	273
τ_{high} (Me_2SO, ms)	N/A	238.1	378.2	458.2	748.1	1307.7
τ_{low} (Me_2SO, ms)	N/A	1564.1	762.2	576.8	363.3	100.0
k_d (Me_2SO, s^{-1})	N/A	4.2	2.6	2.2	1.3	0.8
k_a (Me_2SO, s^{-1})	N/A	0.6	1.3	1.7	2.8	10.0
τ_{high} (H_2O, ms)	N/A	188.2	312.0	486.8	679.5	1350.0
τ_{low} (H_2O, ms)	N/A	1285.9	560.5	300.3	186.8	120.9
k_d (H_2O, s^{-1})	N/A	5.3	3.2	2.1	1.5	0.7
k_a (H_2O, s^{-1})	N/A	0.8	1.8	3.3	5.4	8.3

table S11. Dissociation (k_d) and association (k_a) rate constants. Dissociation (k_d) and association rate constants (k_a) of pseudorotaxane MV^{2+}⊂BPP34C10 from time interval results of the thrid device at five different temperatures in Me_2SO and aqueous solutions, respectively. The dwell time of their "high" and "low" states (τ_{high} and τ_{low}) were also calculated.

T (K)	323	313	303	293	283	273
τ_{high} (Me_2SO, ms)	N/A	231.3	271.9	561.5	854.1	1276.6
τ_{low} (Me_2SO, ms)	N/A	1307.9	697.1	599.0	316.2	126.3
k_d (Me_2SO, s^{-1})	N/A	4.3	3.7	1.8	1.2	0.8
k_a (Me_2SO, s^{-1})	N/A	0.8	1.4	1.7	3.2	7.9
τ_{high} (H_2O, ms)	N/A	218.8	363.9	535.8	772.3	1463.0
τ_{low} (H_2O, ms)	N/A	1158.3	649.8	330.1	204.7	98.0
k_d (H_2O, s^{-1})	N/A	4.6	2.8	1.9	1.3	0.7
k_a (H_2O, s^{-1})	N/A	0.9	1.5	3.0	4.9	10.2

table S12. Dissociation (k_d) and association (k_a) rate constants. Dissociation (k_d) and association rate constants (k_a) of pseudorotaxane MV^{2+}⊂BPP34C10 from time interval results of the forth device at five different temperatures in Me_2SO and aqueous solutions, respectively. The dwell time of their "high" and "low" states (τ_{high} and τ_{low}) were also calculated.

T (K)	323	313	303	293	283	273
τ_{high} (Me_2SO, ms)	N/A	189.9	381.2	481.6	731.6	1283.2
τ_{low} (Me_2SO, ms)	N/A	1486.2	791.1	560.6	228.7	138.8
k_d (Me_2SO, s^{-1})	N/A	5.3	2.6	2.1	1.4	0.8
k_a (Me_2SO, s^{-1})	N/A	0.7	1.3	1.8	4.4	7.2
τ_{high} (H_2O, ms)	N/A	146.9	253.5	417.9	643.9	1403.8
τ_{low} (H_2O, ms)	N/A	1207.2	607.8	337.2	191.0	77.5
k_d (H_2O, s^{-1})	N/A	6.8	4.0	2.4	1.6	0.7
k_a (H_2O, s^{-1})	N/A	0.8	1.7	3.0	5.2	12.9

table S13. Dissociation (k_d) and association (k_a) rate constants. Dissociation (k_d) and association rate constants (k_a) of pseudorotaxane MV^{2+}⊂BPP34C10 from time interval results of the fifth device at five different temperatures in Me_2SO and aqueous solutions, respectively. The dwell time of their "high" and "low" states (τ_{high} and τ_{low}) were also calculated.

T (K)	323	313	303	293	283	273
τ_{high} (Me_2SO, ms)	N/A	190.5	377.2	453.1	726.9	1576.4
τ_{low} (Me_2SO, ms)	N/A	1442.6	807.1	643.6	323.9	131.3
k_d (Me_2SO, s^{-1})	N/A	5.3	2.7	2.2	1.4	0.6
k_a (Me_2SO, s^{-1})	N/A	0.7	1.2	1.6	3.1	7.6
τ_{high} (H_2O, ms)	N/A	165.6	280.7	393.4	620.3	1663.1
τ_{low} (H_2O, ms)	N/A	1340.5	678.0	298.4	233.5	92.9
k_d (H_2O, s^{-1})	N/A	6.0	3.6	2.5	1.6	0.6
k_a (H_2O, s^{-1})	N/A	0.8	1.5	3.4	4.3	10.8

table S14. Dissociation (k_d) and association (k_a) rate constants. Dissociation (k_d) and association rate constants (k_a) of pseudorotaxane MV^{2+}⊂BPP34C10 for the results of mean (M) and standard deviation (SD) from time interval results measured from all five devices at five different temperatures (313 K, 303 K, 293 K, 283 K, and 273 K) in Me_2SO and aqueous solution, respectively.

T (K)	323	313	303	293	283	273
k_d (M, Me_2SO)	N/A	4.7	2.9	2.1	1.3	0.7
k_d (SD, Me_2SO)	N/A	0.7	0.5	0.2	0.1	0.1
k_a (M, Me_2SO)	N/A	0.7	1.3	1.7	3.4	8.5
k_a (SD, Me_2SO)	N/A	0.1	0.1	0.1	0.6	1.2
k_d (M, H_2O)	N/A	5.9	3.5	2.3	1.5	0.7
k_d (SD, H_2O)	N/A	1.0	0.5	0.2	0.2	0.1
k_a (M, H_2O)	N/A	0.8	1.8	3.2	5.1	11.2
k_a (SD, H_2O)	N/A	0.1	0.4	0.2	0.5	2.1

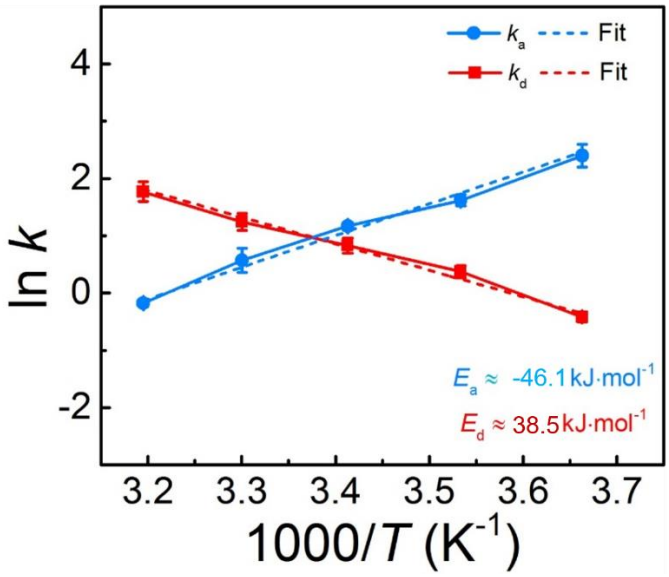

fig. S20. Host-guest kinetics analysis. Arrhenius plots of association ($k_a = 1/\tau_{low}$) and dissociation ($k_d = 1/\tau_{high}$) rate constants deduced ($E_a \approx -46.1$ kJ·mol^{-1} and $E_d \approx 38.5$ kJ·mol^{-1}).

13. Computational Analyses

The geometric optimizations for graphene-based electrode systems of BPP34C10 and MV^{2+}⊂BPP34C10 complex (fig. S21), which mimic the experimental molecular junctions, were performed using semi-empirical methods AM1 within Gaussian 03 package. The calculated conformation and co-conformation are consistent with previous crystallographic data (*44*, *45*). Once the molecular structure is relaxed, DFT was employed to compute the molecular orbitals. The hybrid functional B3LYP (*41*) with a basis set of 6-31+G* was used.

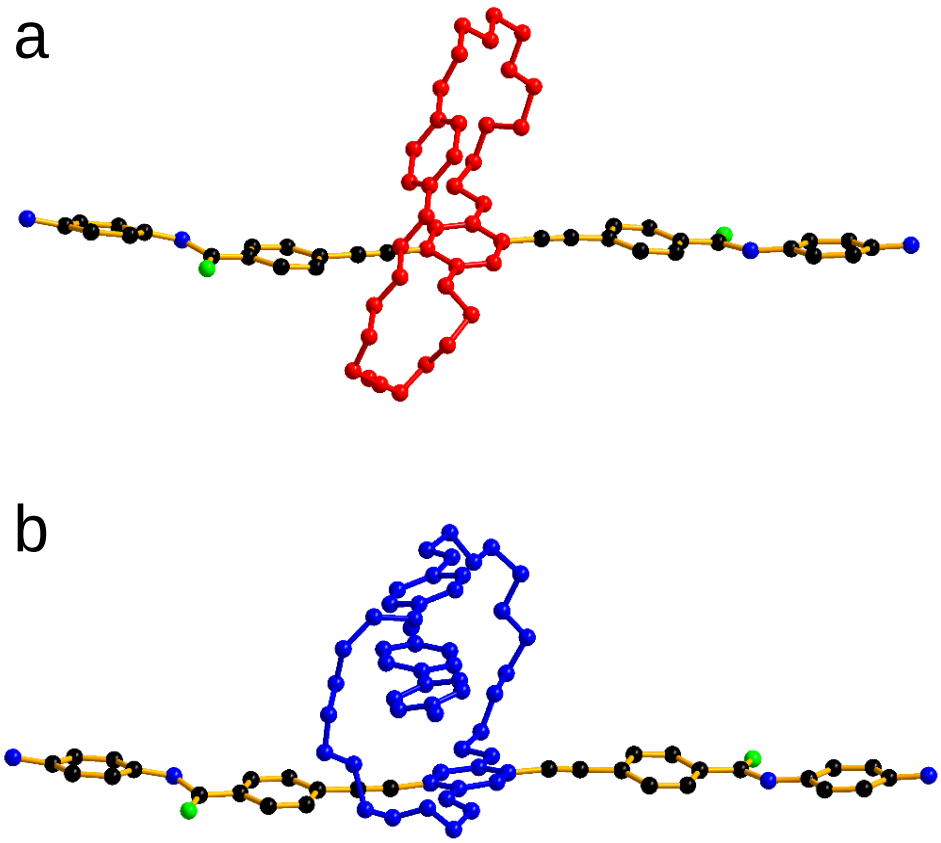

fig. S21. Geometric optimizations of BPP34C10 and MV^{2+}⊂BPP34C10 complexes. The optimized (co)conformations of (**a**) BPP34C10 and (**b**) MV^{2+}⊂BPP34C10 at the B3PW91/6-31+G*/Lanl2dz(*f*) level, consistent with previous crystallographic data. Counterions and hydrogen atoms were omitted for simplicity.

The transmission spectra were calculated within the framework of density functional theory combined with equilibrium Green's function method within the Atomistix toolkit package (*42*, *43*). The local density approximation exchange-correlation functional and the double zeta basis were used. The kinetic energy cutoff was chosen to be 100 Ha. The sampling of the Brillouin zone was 10 × 10 × 100 according to the Monkhorst-Pack (MP) scheme. For each sate of BPP34C10- or

MV^{2+}⊂BPP34C10-SMJ, the transmission peaks matched the molecular orbitals and molecular projected self-consistent Hamiltonian (MPSH) (*46*) spectra (Fig. 3). When a bias voltage was applied, the electron distribution changed, and some peaks began to merge with the transmission windows, which led to the conductance increase.